

Broad Ne VIII $\lambda 774$ Emission From Quasars

FRED HAMANN¹, ROSS D. COHEN

*The Center for Astrophysics and Space Sciences, University of California – San Diego,
La Jolla, CA 92093-0424*

JOSEPH C. SHIELDS

Department of Physics and Astronomy, Ohio University, Athens, OH 45701-2979

E. M. BURBIDGE, VESA JUNKKARINEN

*The Center for Astrophysics and Space Sciences, University of California – San Diego,
La Jolla, CA 92093-0424*

D. M. CRENSHAW

Goddard Space Flight Center, Code 681, Greenbelt, MD 20771

ABSTRACT

Ne VIII $\lambda 774$ is an important tracer of the high-ionization gas in QSOs. We examine the Ne VIII emission-line properties using new *HST*-FOS spectra of four sources, mean spectra derived from two QSO samples in the *HST* archives, and new photoionization calculations. The results support our previous claim that broad Ne VIII lines are common in QSOs, with an average flux of $\sim 42\%$ of O VI $\lambda 1034$ and velocity widths that are ~ 2 to 5 times larger than O VI, C IV $\lambda 1549$ and other broad lines in the same spectra. The strongest and most reliably measured Ne VIII $\lambda 774$ lines (in two sources) have FWHM $\sim 14,500$ km s⁻¹. Line profile fits in these cases show that the unusually large widths might be caused by blending with emission from N IV $\lambda 765$ and O IV $\lambda 789$. However, standard photoionization calculations indicate that N IV, O IV and all other lines near this wavelength should be too weak, leaving (very broad) Ne VIII as the only viable identification for the ~ 774 Å feature. (This conclusion might be avoided if there are large radial velocity dispersions [$\gtrsim 1000$ km s⁻¹] in the emitting region and the resonant absorption of continuum photons enhances the flux in weaker lines.) The calculations also indicate that the Ne VIII emitting regions have ionization parameters in the range $5 \lesssim U \lesssim 30$, total hydrogen column densities of $10^{22} \lesssim N_{\text{H}} \lesssim 3 \times 10^{23}$ cm⁻², and an average covering factor of $\gtrsim 30\%$ (for solar abundances and a nominal QSO continuum shape). The Ne VIII emitting region is therefore more extensive, more highly ionized, and has much higher velocities than the rest of the broad emission line region (BELR). This highly-ionized BELR component would be a strong X-ray “warm” absorber if it lies along our line-of-sight to the X-ray continuum source.

Subject headings: Galaxies: Quasars: emission lines – Galaxies: Quasars: general

¹email: fhamann@ucsd.edu

1. Introduction

The rest-frame UV spectra of QSOs and active galactic nuclei (AGNs) typically contain strong and broad emission lines (BELs) from the resonance doublets C IV $\lambda 1549$, N V $\lambda 1240$ and O VI $\lambda 1034$ in the lithium-like isoelectronic sequence. Ne VIII $\lambda 774$ is another resonant doublet in that sequence. Its short wavelength makes $\lambda 774$ difficult to measure, but this line deserves special attention because Ne VIII requires ionization energies (207 eV) nearly twice as large as O VI (114 eV) and more than four times larger than C IV (48 eV). Broad Ne VIII $\lambda 774$ lines can therefore probe the extreme high-ionization gas in the broad emission line regions (BELRs) and test the possible relationship of this gas to other high-ionization phenomena in QSO/AGN environments. For example, the Ne VIII-emitting BELR has an ionization consistent with the X-ray “warm” absorbers (Halpern 1984) observed in some quasars and AGNs. Warm absorbers can be identified by bound-free edges of O VII and O VIII near 0.8 keV (for example, George *et al.* 1997, Reynolds 1997, Otani *et al.* 1996, Mihara *et al.* 1994, Fabian *et al.* 1994, Turner *et al.* 1993a). Photoionization calculations indicate that the regions producing Ne VIII line emission would also produce these edges in soft X-rays if the gas lies along our line-of-sight to the X-ray continuum source (Netzer 1993, Hamann *et al.* 1995a, Shields *et al.* 1995, Reynolds & Fabian 1995, Netzer 1996).

There are now several reports of broad $\lambda 774$ emission from QSOs (Cohen *et al.* 1994, Hamann *et al.* 1995a, Zheng *et al.* 1997, Hamann, Zuo & Tytler 1995b), but the data are often of poor quality and the number of secure detections is small. Hamann *et al.* (1995b) made the first attempt to study the general strength and character of Ne VIII $\lambda 774$ emission in a sample of QSOs. That sample consists of 5 radio-loud and radio-quiet sources measured in the *Hubble Space Telescope* (*HST*) Absorption Line Snapshot Survey (Absnap). They found that 3 of the 5 sources, and possibly all 5, have a BEL at ~ 774 Å. They argued that the measured wavelengths and fluxes (compared to photoionization models) both point to Ne VIII $\lambda 774$ as the most likely identification. More recently, Zheng *et al.* (1997) measured the ~ 774 Å emission line in a composite spectrum derived from a larger number of QSOs.

Here we supplement that work with new photoionization calculations and new *HST* and ground-based

spectroscopy of four QSOs. We also extract an unbiased sample of 11 QSOs from the *HST* archives and combine them with our previous Absnap sample to construct mean spectra for a total of 16 sources. The new individual spectra provide the highest signal-to-noise measurements of the Ne VIII feature, while the means allow us to study the Ne VIII $\lambda 774$ emission properties in representative samples. Section 2 below describes the observations and measurements of the emission lines. Section 3 reexamines the Ne VIII $\lambda 774$ identification and provides an analysis of the kinematics and physical conditions based on photoionization simulations and fits to the line profiles. Section 4 discusses the implications of the Ne VIII $\lambda 774$ emission and, in particular, the possible relationship to warm absorbers. Section 5 provides a summary.

2. The Data

2.1. Observations and Target Selection

We obtained UV spectra of four bright QSOs with the Faint Object Spectrograph (FOS) on board *HST*. We observed PKS 0355–483 and Q 1435–015 because they were strong candidates for broad Ne VIII $\lambda 774$ emission in our previous study of the *HST*-Absnap sample (Hamann *et al.* 1995b). We chose PG 1148+549 as another candidate for strong Ne VIII emission based on earlier observations with the *International Ultraviolet Explorer* (*IUE*; Hamann *et al.* 1995a). We observed the QSO PG 1522+101 as part of an unrelated absorption-line study and include it here because the *HST* spectra contain a strong emission line near 774 Å rest (Cohen *et al.* 1994).

The *HST* spectra encompass Ne VIII $\lambda 774$ and other prominent lines in the rest frame UV but, for the two highest-redshift sources, Q 1435–015 and PG 1522+101, they do not include the important C IV $\lambda 1549$ line. We therefore obtained ground-based optical spectra of these QSOs with the Shane 3.0 m telescope at Lick Observatory. Table 1 provides a log of the observations, including the dates, the telescopes used (Tel.), the spectrographs and their setups/gratings (Instr./Setup), the wavelengths covered (λ_{obs}), the approximate full-width-at-half-maximum resolutions $R \equiv \lambda/\Delta\lambda$, and the total exposure times (Exp.). The emission-line redshifts listed with the QSO names are from Hewitt & Burbidge (1993), except for PG 1148+549, which is from Schmidt & Green (1983). The *HST*-FOS spectra were obtained through the 1'' science aperture and calibrated at

the *Space Telescope Science Institute* using their standard “pipeline” procedures. We recalibrated the absolute wavelengths in the G130H and G270H spectra by requiring that Galactic absorption lines appear at their laboratory wavelengths. We then shifted the G190H or G160L spectra by matching features in spectral regions that overlap with G130H or G270H. We expect that the final 3σ wavelength uncertainties are less than 0.5 diodes, that is $\lesssim 4 \text{ \AA}$ with the G160L grating and $\lesssim 0.5\text{--}1 \text{ \AA}$ with the higher resolution gratings. The Lick observations employed a $2''$ slit and a 400×1200 Reticon CCD. We reduced those data in the usual way using VISTA software (modified slightly by Dr. T. A. Barlow). The wavelength uncertainties in the Lick spectra should be less than $\sim 0.2 \text{ \AA}$. We flux-calibrated those spectra by observing both the QSOs and standard stars through a wide slit on the same night. None of the data are corrected for Galactic extinction. We simply note that for a typical high-latitude Galactic column density of $N_H = 3 \times 10^{20} \text{ cm}^{-2}$ (Murphy *et al.* 1995 and references therein), a conversion factor of $E(B-V) = N_H / (4.93 \times 10^{21} \text{ cm}^{-2})$ (Diplas & Savage 1994) and a typical extinction curve with $R_V = 3.1$ (Cardelli, Clayton & Mathis 1989), the extinction peak at the $\sim 2175 \text{ \AA}$ silicate feature is roughly 0.5^m . This peak coincides with the O VI $\lambda 1034$ emission line for $z_e = 1.10$.

Figures 1–4 plot the new and old spectra together. The new *HST* observations of PKS 0355–483 and Q 1435–015 (Figures 1 and 3) have higher signal-to-noise ratios and slightly higher resolutions than the Absnap data because of the longer exposure times and improved line spread function of the post-COSTAR FOS. Figure 2 includes two versions of the *IUE* spectrum of PG 1148+549 for comparison to the *HST* data. The bottom spectrum in that figure, labeled “old *IUE*”, is the original data as shown in Hamann *et al.* (1995a). The middle spectrum, labeled “new *IUE*”, is a new reduction of the same data. The old *IUE* spectrum was reduced using an optimal extraction technique (Kinney *et al.* 1991, Lanzetta *et al.* 1993). The new *IUE* spectrum derives from the improved image processing system (NEWSIPS) used for the *IUE* Final Archives (Nichols & Linsky 1996) and is the average from three separate images that have been cleaned of cosmic rays. The new *IUE* reduction of PG 1148+549 has a slightly higher signal-to-noise ratio, but there is a camera artifact at $\sim 1663 \text{ \AA}$ (Crenshaw *et al.* 1990) that is enhanced by NEWSIPS.

The Ne VIII emission line discussed by Hamann *et al.* (1995a) is weaker in both the NEWSIPS reduction and the *HST* spectrum (upper curve in Figure 3).

Figure 4 plots the low (G160L) and high (G190H+G270H) resolution *HST* spectra of PG 1522+101, with the longer wavelength Lick Observatory data appended to the latter. Both *HST* observations of this source show strong $\sim 774 \text{ \AA}$ emission, but the higher resolution spectrum shows more clearly the “forest” of Ly α absorption lines shortward of the QSO’s Ly α emission. These absorption features can significantly distort the continuum and BELs in low resolution data. There is also weak Lyman limit absorption in this spectrum at $\sim 1980 \text{ \AA}$ (observed), which is confirmed by detection of the corresponding Lyman series lines.

2.2. Mean Spectra

We constructed mean spectra of two samples of QSOs measured with *HST*-FOS and the low-resolution grating (G160L). The first sample consists of the 5 QSOs selected by Hamann *et al.* (1995b) from the *HST*-Absnap database (Tytler & Zuo 1994). That sample includes QSOs with (1) emission redshifts ($z_e \approx 0.75$ to 1.4) that allow wavelength coverage across both Ne VIII $\lambda 774$ and O VI $\lambda 1034$ with the G160L grating, (2) no Lyman-limit absorption across $\sim 774 \text{ \AA}$ in the QSO rest frame, and (3) subjectively “measurable” O VI emission. The last criterion serves as a signal-to-noise discriminator and insures that we can establish an emission redshift for coadding the spectra. This selection based on O VI could introduce a bias toward sources with more high-ionization gas and thus stronger O VI and Ne VIII emission lines (see §2.4 below). However, the QSOs were *not* chosen for their Ne VIII characteristics.

The second sample consists of 11 QSOs from the first *HST* Absorption Line Key Project database (Bahcall *et al.* 1993) selected by criteria (1) and (2) above². Seven of these QSOs have measurable O VI emission and 4 do not. We will refer to the subset of 7 Key Project spectra with significant O VI as KP-sub, and the full sample of 11 Key Project spectra as KP-full³. Note that none of the spectra that lack O VI

²We excluded a 12th object from the Key Project sample, PG 1407+265, even though it meets both criteria 1 and 2. This peculiar object has extremely weak lines (we estimate REW(O VI) and $\text{REW(Ly}\alpha)$ $< 6 \text{ \AA}$ at 3σ) and a poorly defined redshift (see McDowell *et al.* 1995).

³The KP-sub sample is the same as what we called “Key Project” in our preliminary report on these data (Hamann *et al.*

emission, including PG 1407+265 (footnote 2), have a detectable Ne VIII line.

Figure 5 plots the mean spectra derived from the various sub-samples and the Total sample of 16 sources. We calculated the means using the new *HST*-FOS spectra of the two Absnap sources PKS 0355–483 and Q 1435–015 (§2.1). The other Absnap spectra are from Hamann *et al.* (1995b). The Key Project spectra are from the *HST* archives with reductions by Schneider *et al.* (1993). PG 1148+549 and PG 1522+101 (§2.1) are not in the Absnap or Key Project samples and so are not included in the means. For the 12 sources with well-defined O VI lines (in the Absnap and KP-sub samples) we shifted the individual spectra to the rest frame by forcing the centroid of the upper $\sim 50\%$ of the O VI profile to be at 1033.8 Å. For the 4 sources without O VI, we shifted the spectra using published redshifts in Hewitt & Burbidge (1993). Applying the published redshifts, which derive from low-ionization lines such as C III] $\lambda 1909$ or Mg II $\lambda 2799$, leads to larger uncertainties (by at least several Å) in the rest wavelengths of O VI and Ne VIII because (1) these redshifts do not compensate for the calibration uncertainties in the *HST*-FOS wavelengths and (2) there are known intrinsic redshift differences between high- and low-ionization lines (Espy *et al.* 1989, Tytler & Fan 1992). In all cases, we normalized the continua to unity by fitting⁴ with low-order polynomials and then averaged the spectra with equal weights. Wavelength regions at the ends of individual spectra were excluded from the means if they contain obvious Lyman-limit absorption, severe noise spikes, or geocoronal emission lines such as Ly α in first or second order. The histogram at the bottom of Figure 5 indicates the number of spectra contributing to the Total mean at each wavelength. Median spectra drawn from these samples are qualitatively the same as the means.

2.3. Line Measurements

Table 2 lists the centroid rest wavelengths (λ_{rest}), rest equivalent widths (REWs), observed fluxes (Flux), and full widths at half maximum (FWHM) for emission lines detected in the new *HST* and Lick spec-

1996), except here we have identified and included one more QSO that meets the sample criteria.

⁴All fitting and arithmetic manipulations were performed with the IRAF software distributed by the National Optical Astronomy Observatories under contract to the National Science Foundation.

tra (Figures 1–4) and in several of the mean spectra (Figure 5). Not all of the lines labeled in Figures 1–5 are present in the data; for example, Mg X $\lambda 615$ and Ne VII] $\lambda 895$ are not detected in any source with approximate 3σ upper limits of REW $\lesssim 2$ Å in all cases. The measurements for PG 1522+101 are from the higher resolution data after interpolating across the strongest of the overlying Ly α forest lines. We made no attempt to correct for absorption lines in the other sources. The fluxes given for the mean spectra are relative to O VI $\lambda 1034$, while those given for the individual sources are as observed with units 10^{-14} ergs s $^{-1}$ cm $^{-2}$. Recall that the data are not corrected for Galactic extinction (§2.1). The equivalent widths are immune to extinction effects, but the fluxes are not. In a worst-case scenario, with the ~ 2175 Å extinction peak overlying the O VI line (§2.1), the differential extinction between O VI and Ne VIII for a typical Galactic column density would be $\sim 0.1^m$ and would lead us to overestimate the true Ne VIII/O VI flux ratio by 10%.

The emission lines were measured by integrating the flux above the fits to the continua (dotted curves in Figures 1–5) between the wavelengths indicated by $\Delta\lambda$ in Table 2. We did not attempt to separate severely blended lines or line components. In particular, the feature we attribute to O VI $\lambda 1034$ could have a contribution from Ly β $\lambda 1026$. Laor *et al.* (1995) and Wills *et al.* (1995) estimate that the mean Ly β contributions to this blend are $\sim 23\%$ and $\lesssim 10\%$, respectively, in samples of low-redshift QSOs measured with *HST*. We will ignore this small contribution in our discussions below. We will also ignore the weak Si II $\lambda 1527$ line that can add to the measured C IV $\lambda 1549$ flux.

The feature we identify as Ne VIII $\lambda 774$ is clearly present in the mean spectra, and it is stronger than the means (both in REW and relative to other lines) in the individual QSOs PKS 0355–483 (radio-loud) and PG 1522+101 (radio-quiet). The observations of Q 1435–015 are less conclusive, but the new data are consistent with the previous report of strong ~ 774 Å emission from this source (Hamann *et al.* 1995b). The new *HST*-FOS spectrum of PG 1148+549 does not exhibit the strong ~ 774 Å line noted in the original *IUE* data (Hamann *et al.* 1995a). The *HST* spectrum of this source resembles the reprocessed (“new”) *IUE* spectrum (Fig. 3), indicating that the Ne VIII line is weaker than our previous claim.

There is evidence in the means and in some of the

individual spectra for emission from the excited-state line C III* $\lambda 1176$ and from a broad unidentified feature at ~ 1070 Å. The unidentified feature was noted previously by Laor *et al.* (1994 and 1995) in their sample of low-redshift QSOs. The C III* line could prove to be a valuable diagnostic of BELR physical conditions because it involves a transition between unusually high energy states, 17.1 to 6.5 eV. The lower state is metastable and gives rise to the well-known C III] $\lambda 1909$ emission line (see Korista *et al.* 1997, Laor *et al.* 1997a for discussion).

2.4. What is the Average ~ 774 Å Line Strength?

Unbiased measurements of the average ~ 774 Å line strength require spectra of many QSOs selected by only their redshifts and their lack of overlying Lyman-limit absorption (criteria 1 and 2 in §2.2). Among the data we collected, the KP-full sample of 11 spectra comes closest to this ideal. The average ~ 774 Å line in that sample has REW ~ 5.9 Å and a flux of $\sim 42\%$ of O VI $\lambda 1034$ (Table 2). These results can be compared to REW ~ 3.2 Å and a flux ratio of $\lambda 774/\lambda 1034 \sim 21\%$ reported by Zheng *et al.* (1997) from their composite *HST* spectrum. The Zheng *et al.* composite includes ~ 20 spectra across ~ 774 Å and 80–90 across the O VI line. Our KP-full sample is undoubtedly a subset of the spectra they used. The different line strengths in these two samples could be caused by random fluctuations in the small numbers of spectra involved and/or by the large measurement uncertainties, which are dominated by the subjective continuum placement. However, the reported differences might also be caused by selection effects. In particular, there is an inherent “Baldwin Effect” in the Zheng *et al.* composite. Several studies have shown that this effect is pervasive in QSO samples; more luminous QSOs have typically lower emission-line REWs (Baldwin 1977, Kinney *et al.* 1990). The spectra in the *HST* database are primarily of the brightest QSOs at each redshift. Our KP-full sample includes a relatively narrow redshift range so that ~ 774 Å through ~ 1034 Å are measured in the same data, but the Zheng *et al.* composite has many more low redshift and low luminosity QSOs contributing at long wavelengths (e.g. across O VI) than at short wavelengths (at Ne VIII). Therefore their composite should have a larger REW in $\lambda 1034$, a smaller REW in $\lambda 774$ and a lower $\lambda 774/\lambda 1034$ strength ratio compared to our KP-full sample, which agrees with the measured results.

Therefore, our KP-full sample, although still limited by the small number of spectra and significant measurement uncertainties, should provide the most representative measure of the $\lambda 774$ line strength and the $\lambda 774/\lambda 1034$ flux ratio in (bright) QSOs at redshift ~ 1 . The Absnap and KP-sub samples both have stronger $\lambda 774$ lines than KP-full, probably because of a selection bias introduced by the requirement for “measurable” O VI emission (§2.2). Note, however, that while $\lambda 774$ is stronger in the Absnap sample, $\lambda 1034$ and the Ly α blend are not; therefore, the nature and extent of the selection bias is ambiguous. The Total mean mixes the Absnap and KP-full samples and therefore has slightly stronger ~ 774 Å line emission than KP-full alone.

3. Analysis

3.1. Photoionization Calculations

Theoretical models of the BELR are needed to understand the conditions under which Ne VIII $\lambda 774$ forms and the likelihood that other lines near this wavelength might contribute to the measured emission. Some recent photoionization calculations have made specific predictions for the Ne VIII line strength (Hamann *et al.* 1995a, Korista *et al.* 1997, Netzer 1996). Here we update the calculations in Hamann *et al.* (1995a) using a newer version of CLOUDY (90.02; Ferland 1996) to examine other strong lines at wavelengths < 1000 Å and test whether recent improvements in the atomic data affect the results (see also Baldwin *et al.* 1996, Korista *et al.* 1997).

3.1.1. Predicted Line Strengths and the Ne VIII Identification

The most likely contributors to broad line emission near 774 Å are Ne VIII $\lambda 774$, N IV $\lambda 765$, O IV $\lambda 789$, S V $\lambda 786$ and Ar VI $\lambda 763$ (Verner, Verner & Ferland 1996). The calculations by Hamann *et al.* (1995a) indicate that the alternatives to Ne VIII should be relatively weak, and therefore Ne VIII is the most likely identification for the measured line. Figure 6 shows the line equivalent widths predicted by CLOUDY for different values of the ionization parameter U (defined as the dimensionless ratio of hydrogen-ionizing photon to hydrogen particle densities at the illuminated face of the clouds). This plot is analogous to Figure 2 in Hamann *et al.* (1995a). The model clouds have a space density of $n_H = 10^{11}$ cm $^{-3}$, a column density of $N_H = 3 \times 10^{23}$ cm $^{-2}$ and solar element abundances.

They are illuminated on one side by a standard QSO spectrum that is believed to be typical of low-redshift QSOs and Seyfert 1 nuclei (Mathews & Ferland 1987). We modified this spectrum to have a sharp decline at wavelengths longer than $2 \mu\text{m}$ to avoid significant free-free heating (Ferland *et al.* 1992). The internal cloud velocities are assumed to be thermal. The equivalent widths in Figure 6 apply for emitting regions that completely cover the central QSO (over 4π ster) but are transparent to the radiation from other clouds (e.g. Ly α and Ne VIII photons emitted on the far side of the QSO are not absorbed or reflected by clouds on the near side).

The effects of different space densities and spectral shapes on some of the line strengths are shown by Korista *et al.* (1997) and Netzer (1996). In general, the relative strengths of the permitted lines in Figure 6 are only weakly dependent on the space density for a given U . The intercombination lines O V] and Ne VII] are strongly suppressed above their common critical density of $\sim 10^{11} \text{ cm}^{-2}$. Smaller column densities would significantly reduce the emission from low- to intermediate-ionization lines (e.g. Ly α , C IV and N V) at the right in Figure 6, because these lines form strictly at large depths in the high- U clouds (see Fig. 3 in Hamann *et al.* 1995a). Examination of the heating and cooling processes indicates that, for the continuum shape used here, clouds with $U \gtrsim 30$ are thermally unstable (Hamann *et al.* 1995a, Netzer 1996).

The only important difference between Figure 6 here and Figure 2 in Hamann *et al.* (1995a) is that the O IV line is now several times stronger, particularly at low and intermediate U ; but the main results are the same. S V $\lambda 786$ and Ar VI $\lambda 763$ are too weak under any circumstances to produce the measured $\sim 774 \text{ \AA}$ line. (The predicted Ar VI $\lambda 763$ line, not shown in Fig. 6, is at least 5 times weaker than S V $\lambda 786$.) The N IV $\lambda 765$ and O IV $\lambda 789$ lines are the strongest alternatives to Ne VIII $\lambda 774$. They form in roughly the same gas as C IV $\lambda 1549$, so their strengths relative to C IV are not sensitive to the uncertain geometry or physical conditions. Scaling the predicted N IV/C IV and O IV/C IV ratios in Figure 6 by the C IV measurements in Table 2 shows that the observed 774 \AA lines in PKS 0355–483 and PG 1522+101 are much too strong to have significant contributions from N IV or O IV. In particular, for $U \lesssim 1$ (see §4), N IV+O IV should have $\text{REW} \lesssim 0.6 \text{ \AA}$ in PKS 0355–483 and $\text{REW} \lesssim 1.9 \text{ \AA}$ in PG 1522+101,

compared to the measured value of $\text{REW} \sim 13.5 \text{ \AA}$ in both QSOs. The ratio of the fluxes predicted in N IV+O IV to that measured in $\sim 774 \text{ \AA}$ is therefore $\lesssim 0.07$ in PKS 0355–483 and $\lesssim 0.3$ in PG 1522+101.

The mean spectra (Fig. 5) do not include C IV $\lambda 1549$ for comparison, but in large ground-based samples C IV has $\text{REW} \sim 20$ to 32 \AA , or about $\sim 50\%$ of Ly α (see the compilation by Hamann & Korista 1996). If we adopt a conservatively large value of $\text{REW}(\lambda 1549) = 40 \text{ \AA}$, then Figure 6 implies that the average N IV+O IV emission should have $\text{REW} \lesssim 1.0 \text{ \AA}$ for $U \lesssim 0.1$ or $\text{REW} \lesssim 3.2 \text{ \AA}$ for $U \lesssim 1$. These estimates are no more than about half the measured mean of $\text{REW} \sim 5.9 \text{ \AA}$ in the $\sim 774 \text{ \AA}$ line (§2.4). Since values of $U \lesssim 0.1$ are generally favored for the C IV emitting region (§4), the average contributions of N IV and O IV to the $\sim 774 \text{ \AA}$ feature should be $\lesssim 17\%$.

These results indicate that Ne VIII $\lambda 774$ dominates the average $\sim 774 \text{ \AA}$ emission and is the only significant contributor whenever this line is strong compared to C IV. Experiments with CLOUDY show that this conclusion holds even if the metallicities are above solar and nitrogen is several times overabundant relative to the other metals (Hamann & Ferland 1992 and 1993).

3.1.2. Ionization, Column Densities and Covering Factors

Figure 6 also supports the conclusions in Hamann *et al.* (1995a) regarding the ionization, column densities and covering factors of the emitting regions. Significant emission in Ne VIII $\lambda 774$, relative to both the continuum and other lines, requires ionization parameters $U \gtrsim 5$. Thermal stability in the clouds independently requires $U \lesssim 30$, for an overall range of $5 \lesssim U \lesssim 30$ in the Ne VIII line-forming gas. The ratio of the observed mean (5.9 \AA ; §2.4) to largest-predicted ($\sim 20 \text{ \AA}$; Fig. 6) $\lambda 774$ equivalent widths implies an average minimum covering factor of $\sim 30\%$. The Ne VIII emitting regions must subtend at least this fraction of the sky as seen from the central QSO to produce the average equivalent width. (The same analysis shows that the strongest Ne VIII emitters, PKS 0355–483 and PG 1522+101, require covering factors $\gtrsim 65\%$.) The observed mean $\lambda 774$ equivalent width also requires a minimum hydrogen column density of $N_H \gtrsim 10^{22} \text{ cm}^{-2}$ for solar abundances, even if the emitting region completely covers the central

QSO (see Figure 3 in Hamann *et al.* 1995a). (The strongest Ne VIII emitters require column densities at least twice as high.) For the range in U values given above, column densities beyond $3 \times 10^{23} \text{ cm}^{-2}$ do not add to the Ne VIII flux, so we have an effective upper limit of $N_H \lesssim 3 \times 10^{23} \text{ cm}^{-2}$ for Ne VIII emission.

These results are uncertain by factors of a few because they depend on the poorly known shape of the ionizing spectrum. The ionization parameter reflects the integrated continuum flux at energies $\gtrsim 13.6 \text{ eV}$, but the Ne VIII ionization depends only on the flux above 207 eV . Therefore, different continuum shapes will yield different estimates of the minimum U value. Netzer (1996) argued that highly ionized species like Ne VIII are best described by an X-ray ionization parameter, U_x , that includes energies between only 0.1 and 10 keV. A similar problem is that the equivalent widths measure the line strengths relative to the *local* continuum (e.g. at 774 \AA), even though that continuum has little to do with the production of Ne VIII $\lambda 774$. Recent calculations by Netzer (1996) predict ~ 3 times lower equivalent widths for $\lambda 774$ compared to Figure 6 because of a softer assumed continuum; the flux ratio $F_\nu(207\text{eV})/F_\nu(774 \text{ \AA})$ is ~ 3 times smaller in Netzer’s (1996) continuum than in the Mathews & Ferland (1987) continuum used in Figure 6. Conversely, experiments with CLOUDY show that harder (flatter) continua, such as the single power law $F_\nu \propto \nu^{-1.4}$ or the “baseline” continuum used by Korista *et al.* (1997), roughly double the peak Ne VIII equivalent width compared to Figure 6 and shift the REW curve to more than 5 times lower U . Even harder power-law continua, such as $F_\nu \propto \nu^{-1.2}$, still only double the peak Ne VIII equivalent width. The ratio of observed ($\sim 5.9 \text{ \AA}$) to largest-predicted ($\sim 40 \text{ \AA}$) equivalent widths in these extreme cases therefore implies a lower limit on the average Ne VIII covering factor of $\sim 15\%$.

3.1.3. A Caveat: Continuum Pumping in High-Velocity Environments

Another uncertainty is the importance of continuum pumping to the line emission. If there are large velocity dispersions along radial lines of sight through the BELR, the resonant absorption of continuum photons can “pump” electrons into upper energy states and significantly enhance the emission line fluxes. This pumping can take two forms, (1) resonant line scattering (absorption and re-emission in

the same transition), and (2) continuum fluorescence (absorption into high energy states followed by cascades through intermediate energy levels). These processes are negligible for metallic lines in “standard” BELR models (e.g. Fig. 6 above) because the continuum photons encounter only thermal line widths in the BELR. However, if there is substantial turbulence or a large range of radial velocities (e.g. in an outflow), the absorption of continuum photons can compete with other excitation mechanisms – particularly in weak resonance lines. Since the velocity field in the BELR is essentially unknown, we consider the possible effects of line scattering and continuum fluorescence here.

The amount of scattering in a given line depends on its velocity width and optical depth as encountered by the continuum radiation. For unblended resonance lines that (1) have no alternate decay routes, (2) are not collisionally deexcited (e.g. at high densities), and (3) are on the flat part of the curve-of-growth (optically thick but no damping wings), the scattering equivalent width resulting from thermal or micro-turbulent gas velocities can be derived by integrating over the saturated absorption line profile. This integration yields

$$W_\lambda^{scat} \approx 2f_c\lambda_o \left(\frac{V_D}{c} \right) \sqrt{\ln \left(\frac{\tau_o}{\ln 2} \right)} \quad , \quad (1)$$

where f_c is the covering factor of the emission region ($0 \leq f_c \leq 1$), λ_o is the line wavelength, τ_o is the line-center optical depth, and V_D is the Doppler velocity (thermal or turbulent). Similarly, radial outflows spanning a velocity range ΔV_r in optically thick lines will produce scattering equivalent widths of

$$W_\lambda^{scat} \approx f_c\lambda_o \left(\frac{\Delta V_r}{c} \right) \quad . \quad (2)$$

Keeping in mind that $\tau_o \propto V_D^{-1}$ in Eqn. 1 and that well-separated doublets like Ne VIII $\lambda\lambda 770, 780$ scatter twice as much flux as single or blended lines, one can use the values of τ_o plotted by Hamann *et al.* (1995a) for strictly thermal velocities to estimate W_λ^{scat} for different values of V_D . Here we use CLOUDY to derive the τ_o directly for models identical to Figure 6 but with larger V_D . We find that for clouds with $U = 10$ and $V_D = 1000 \text{ km s}^{-1}$, the Ne VIII doublet has $W_\lambda^{scat} \sim 25f_c \text{ \AA}$. Similarly, for $U = 0.1$ and $V_D = 1000 \text{ km s}^{-1}$, C IV $\lambda 1549$ has $W_\lambda^{scat} \sim 30f_c \text{ \AA}$ and the N IV $\lambda 765$ and O IV $\lambda 789$ lines both have $W_\lambda^{scat} \sim 10f_c \text{ \AA}$.

Continuum fluorescence will enhance the line emission further via cascades from upper energy states. The importance of fluorescence versus scattering emission for a given line depends on the number of pumping transitions available to higher states, the optical depths in those transitions, the shape of the incident continuum, and the branching ratios (including escape probabilities) out of the upper states (see also Ferguson, Ferland & Pradhan 1995). Experiments with multi-level atoms in CLOUDY indicate that the equivalent widths due to scattering *and* fluorescence are factors of ~ 1.5 to ~ 2 larger than the estimates above for scattering alone.

If we add these illustrative scattering+fluorescence equivalent widths to the REWs in Figure 6, we would derive lower minimum covering factors and minimum column densities for the Ne VIII $\lambda 774$ emitting region by factors of a few compared to §3.1.2. More importantly, the predicted contributions of N IV $\lambda 765$ and O IV $\lambda 789$ to the measured ~ 774 Å lines would be several times larger than our estimates in §3.1.1, because the theoretical ratio of N IV+O IV to C IV emission becomes larger. Therefore, Ne VIII $\lambda 774$ might not dominate the average ~ 774 Å emission if there are large radial velocity dispersions that induce substantial continuum pumping. A thorough analysis of this possibility is beyond the scope of the present paper; we note simply that continuum pumping should also enhance the emission in other weak lines. Future studies might test the continuum pumping hypothesis by examining these weak lines and looking for correlations with the measured ~ 774 Å feature. For example, strong continuum pumping in N IV $\lambda 765$ and O IV $\lambda 789$ at $U \sim 0.1$ should be accompanied by strong pumped emission from C III $\lambda 977$, N III $\lambda 991$ and O III $\lambda 834$. Similarly, strong pumping contributions to Ne VIII $\lambda 774$ at $U \sim 10$ should come with highly pumped Mg X $\lambda 615$ emission and an Mg X/Ne VIII flux ratio that is closer to unity than in Figure 6. Our limited CLOUDY experiments with $V_D = 1000$ km s $^{-1}$ did not reveal any significant discrepancies with the data that would immediately rule out or require large pumping contributions.

3.2. Line Profiles and Redshifts

3.2.1. PKS 0355–483, Q 1435–015 and PG 1522+101

The *HST* spectra of PKS 0355–483 and PG 1522+101 (Figs. 1 and 4) have the strongest and most reliably measured emission lines near 774 Å. Figures 7 and 8

show that their Ly α , C IV, N V and O VI emission lines all have similar profiles. The only significant difference is that N V and O VI are broader than C IV in PKS 0355–483. This small difference might be due to either the larger doublet separations in N V and O VI (see Fig. 7) or small differences in the velocities in their emitting regions. In contrast, the ~ 774 Å features in both QSOs are dramatically broader than the other BELs (see also Table 2). Figure 9 shows similar results for Q 1435–015, although in this case comparisons with the ~ 774 Å line are more uncertain. Overall, we measure FWHMs in the ~ 774 Å feature that are roughly 2 to 5 times larger than C IV and the other BELs in the same spectra (Table 2).

Figures 10 and 11 show our attempts at fitting the ~ 774 Å features in PKS 0355–483 and PG 1522+101 using the measured C IV profiles as templates. We constructed the templates by smoothing the C IV profiles without correcting for the C IV doublet separation (because it is relatively small, ~ 500 km s $^{-1}$). The top panels in Figures 10 and 11 show the best fits assuming that Ne VIII is the only contributor to the measured feature and both of the Ne VIII doublet members (770 and 780 Å) have the same redshift and profile as C IV. The only freely varied parameters were the line strengths. The best fits were determined by χ^2 minimization (with the narrow Ly α forest lines excluded from the minimization in PG 1522+101).

The Ne VIII-only fits show that the ~ 774 Å features are consistent with Ne VIII emission at the C IV redshifts (see also Table 2 and Figs. 7–9 above). In PKS 0355–483 the redshifts of these lines are indistinguishable. In PG 1522+101 the purported Ne VIII line is redshifted by up to ~ 2000 km s $^{-1}$ with respect to the C IV peak, but this shift might not be significant given the profile and centroid uncertainties in the broad ~ 774 Å feature. The much more significant result is that the C IV profiles are far too narrow to explain the ~ 774 Å features in terms of Ne VIII. The lower two panels in Figures 10 and 11 plot the best fits with large contributions from N IV $\lambda 765$ and O IV $\lambda 789$. These fits assume that N IV and O IV also have the same redshift and profile as C IV, with the fluxes freely varied. The results using N IV $\lambda 765$ and O IV $\lambda 789$ alone (middle panels) account better for the overall width of the ~ 774 Å features but they do not match the profile shapes. Fits using N IV and O IV together with the two Ne VIII doublet members (bottom panels) are much better, but we reiterate the conclusion from §3.1; N IV $\lambda 765$ and O IV $\lambda 789$ should

be much weaker than they are portrayed in Figures 10 and 11, unless continuum pumping controls the line excitation.

If the observed ~ 774 Å features are dominated by Ne VIII, the velocity profiles must be substantially broader than C IV and other BELs in the same spectra. We can estimate the widths of the individual Ne VIII doublet components by fitting the ~ 774 Å emission in PKS 0355–483 and PG 1522+101 with one gaussian for each Ne VIII doublet member. For these fits we require that the two gaussian components have the same redshift and velocity width, but the values of those parameters and the strengths of the lines are all freely varied. The results (shown in Figure 12) match the data reasonably well; the fit profiles are only slightly more centrally peaked than the observed Ne VIII lines. In both QSOs, the observed lines are fit slightly better by a 1:1 doublet ratio, but 2:1 ratios are not ruled out. The centroids of the fits are within 0.3 Å of the values listed in Table 2 and the individual components have FWHM $\sim 14,000$ km s $^{-1}$ in both QSOs. This velocity width is similar to the FWHMs measured directly from the profiles (Table 2).

These results imply that the velocities in the Ne VIII region are 2–5 times larger than in the C IV-emitting gas. To understand how much of the Ne VIII flux might come from the lower-velocity C IV gas, we performed additional fits to the PKS 0355–483 and PG 1522+101 profiles using (1) the C IV template at the C IV redshift (as in the top panels of Figs. 10 and 11) plus (2) a gaussian Ne VIII doublet with freely-varied width and redshift (as in Fig. 12). For both QSOs the χ^2 minimization forced the C IV template contributions to zero, yielding fits identical to Fig. 12. Therefore, to first order, the measured profiles suggest emission from a high-velocity region with little or no contribution from the C IV-emitting gas.

3.2.2. Mean Spectra

We did not fit the Ne VIII $\lambda 774$ profiles in the mean spectra because they might be broadened by uncertainties in the measured redshifts and by real redshift differences between Ne VIII and the other lines. Also, our selection requirement for measurable O VI emission might bias the Absnap and KP-sub samples toward more “peaky” O VI line profiles. Nonetheless, we note that the mean Ne VIII profiles are comparable to those in PKS 0355–483 and PG 1522+101 and more than twice as broad as both O VI and Ly α

(Table 2). Although possibly spurious, this result is consistent with the individual QSOs discussed above. We also note that the ~ 774 Å centroid is slightly redshifted in the mean spectra (by ~ 1000 km s $^{-1}$) with respect to the O VI peak (Table 2); however, this velocity shift is probably smaller than the uncertainties.

4. Implications of Strong and Broad Ne VIII $\lambda 774$ Emission

The ionization parameters ($5 \lesssim U \lesssim 30$) and covering factors ($\gtrsim 30\%$) derived for the Ne VIII emitting region (§3.1.2) are both considerably larger than estimates based on low- to intermediate-ionization lines such as Ly α , Mg II $\lambda 2799$, and C IV $\lambda 1549$. In particular, the latter lines indicate $U \lesssim 0.2$ (Davidson & Netzer 1979, Kwan & Krolik 1981, Ferland *et al.* 1992, Shields & Ferland 1993, Baldwin *et al.* 1996), while values as high as $U \sim 2$ have been inferred when O VI $\lambda 1034$ is also considered (Hamann & Ferland 1992). The covering factor of the low-ionization region is expected to be $\lesssim 10\%$ based on both the ratio of observed to predicted Ly α equivalent widths and the infrequency of Lyman limit absorption edges at the emission redshift (see Osterbrock 1986). The much larger covering factor of the Ne VIII region implies that the high-ionization gas is optically thin in the H I Lyman continuum (otherwise it would overproduce the Ly α emission). Optically thin, high-ionization clouds have been proposed before to explain the strength of the N V and O VI lines (Davidson & Netzer 1979), and there is evidence from AGN variability studies that part of the C IV $\lambda 1549$ emission comes from optically thin gas (see Shields *et al.* 1995 and references therein). Our Ne VIII results suggest that the highest ionization lines have the largest contributions from optically thin gas. George, Turner & Netzer (1995) reached a similar conclusion based on the tentative detection of a large O VII line equivalent width in X-ray spectra of the Seyfert 1 galaxy NGC 3783.

In spite of the low optical depths near the Lyman limit, the Ne VIII-emitting gas has a substantial opacity to soft X-rays. Our calculations show that O VII and O VIII are the dominant species of oxygen in the Ne VIII-emitting region (see, for example, Fig. 3 in Hamann *et al.* 1995c). The minimum column density of $N_H \gtrsim 10^{22}$ cm $^{-2}$ (§3.1.2) implies a minimum column in O VII+O VIII of $N_O \gtrsim 10^{19}$ cm $^{-2}$. The resulting optical depth through the Ne VIII gas

is $\tau \gtrsim 1$ at the O VII or O VIII edges (based on photoionization cross-sections in Osterbrock 1989). Therefore, the Ne VIII component of the BELR would be a strong warm absorber, characterized by O VII+O VIII edges at ~ 0.8 keV, if it lies along our line of sight to the X-ray continuum source (see also Netzer 1993, Hamann *et al.* 1995a, Shields *et al.* 1995, Netzer 1996). Moreover, the range of physical conditions needed for strong Ne VIII emission, $5 \lesssim U \lesssim 30$ and $10^{22} \lesssim N_H \lesssim 3 \times 10^{23} \text{ cm}^{-2}$ (§3.1.2), encompasses the specific conditions estimated for several strong warm absorbers (e.g. Mathur, Wilkes & Aldcroft 1997, George *et al.* 1997, Otani *et al.* 1996, George *et al.* 1995, Fiore *et al.* 1993). The broad Ne VIII $\lambda 774$ lines reported here clearly identify a BELR component with warm absorber properties.

These results support models in which the warm absorbers are part of, or closely related to, the BELR (e.g. Reynolds & Fabian 1995, Netzer 1996 and references therein). Other studies suggest that warm absorbers are also closely related to the blueshifted absorption lines observed in some QSOs and Seyfert galaxies (Mathur 1994, Mathur *et al.* 1994, Mathur *et al.* 1995, Shields & Hamann 1997). These absorption lines form in outflows with line-of-sight velocities ranging from near zero to $\gtrsim 20,000 \text{ km s}^{-1}$ (e.g. in the broad absorption line [BAL] systems; Foltz *et al.* 1988, Ulrich 1988, Weymann *et al.* 1991). There is no direct evidence for outflow in the Ne VIII $\lambda 774$ emission-line data, but the ultra-broad line widths reported here, with FWHM $\sim 14,500 \text{ km s}^{-1}$ in two well-measured cases, are consistent with high velocities in the warm absorber gas. The large Ne VIII FWHMs are also consistent with emission from the “very broad line region” (VBLR), which was identified by Ferland, Korista & Peterson (1990) from the non-varying H α line wings in a Seyfert 1 galaxy. Ferland *et al.* (1990) present independent arguments that the VBLR is highly ionized, optically thin at the Lyman limit and the likely source of X-ray warm absorption (see also Marziani & Sulentic 1993).

The large covering factors and warm absorber-like properties of the Ne VIII emitting regions suggest that warm absorbers should be common in QSOs. The most recent X-ray surveys indicate that warm absorbers are common in Seyfert 1 nuclei (with a $\gtrsim 50\%$ detection rate; Turner & Pounds 1989, Turner *et al.* 1993b, Nandra & Pounds 1994, Reynolds 1997, George *et al.* 1997) but *rare* in QSOs ($\sim 5\%$ detection rate; Laor *et al.* 1997b). The rarity of

warm absorbers in QSOs might be reconciled with the Ne VIII emission-line data if (1) QSO ionizing spectra are harder than the Mathews & Ferland (1987) continuum, requiring smaller Ne VIII covering factors (§3.1.2), (2) large radial velocity dispersions ($\gtrsim 1000 \text{ km s}^{-1}$) in the BELR enhance the emission in Ne VIII $\lambda 774$ and other weak lines via continuum pumping (§3.1.3), or (3) QSOs are observed over limited viewing angles that usually avoid Ne VIII gas along our line-of-sight to the X-ray continuum source. Viewing angles that avoid the BELR might occur naturally in the recent disk-wind models (Murray & Chiang 1995, Murray *et al.* 1995). In these models, all of the BELs form close to the accretion disk and the highest ionization lines form at the smallest disk radii. Murray (1996) pointed out that the exceptionally broad Ne VIII $\lambda 774$ profiles might be due to enhanced rotational broadening associated with the inner disk. However, that interpretation might conflict with our estimates of large Ne VIII covering factors, which require substantial emission from regions away from the disk plane. Better data and more specific comparisons with the models are needed before drawing firm conclusions.

The large Ne VIII $\lambda 774$ line widths compared to C IV $\lambda 1549$ and especially O VI $\lambda 1034$ might provide strong constraints on models of the emitting regions in general. The calculations in Figure 6 indicate that the gas producing the ultra-broad Ne VIII line should also produce considerable O VI emission. This ultra-broad component to the O VI lines might be hard to hide in the measured profiles, particularly for sources like PKS 0355–483 where any high-velocity O VI emission must be weak compared to Ne VIII $\lambda 774$ (Figs. 1 and 7). However, we can lower the predicted O VI/Ne VIII flux ratio by adopting large values of U and/or lower N_H compared to that used in Figure 6. (Adding continuum pumping via large turbulent velocities [§3.1.3] does not significantly alter the O VI/Ne VIII flux ratio.) Limited experiments with CLOUDY indicate that O VI $\lambda 1034$ can be ~ 2 or more times weaker than Ne VIII $\lambda 774$ if $U \geq 20$ and $N_H \leq 3 \times 10^{22} \text{ cm}^{-2}$. Larger gas densities and/or different ionizing continuum shapes can further reduce the theoretical O VI/Ne VIII flux ratio (see also Korista *et al.* 1997). Alternatively, or perhaps in addition, the measured $\sim 774 \text{ \AA}$ lines might be broadened by blending with N IV $\lambda 765$ and O IV $\lambda 789$ if their emission is enhanced by continuum pumping (§§3.1.3 and 3.2.1). In that case, the true Ne VIII line widths

could be comparable to the other BELs and there would be no need for an ultra-high velocity Ne VIII emitting region.

5. Summary

The mean spectrum of an unbiased sample (KP-full) of 11 radio-loud and radio-quiet QSOs clearly shows broad-line emission at ~ 774 Å with an average REW of ~ 5.9 Å and an average flux equal to $\sim 42\%$ of O VI $\lambda 1034$. This result supports our previous conclusion (based on a smaller sample) that ~ 774 Å emission is common in QSOs. New *HST*-FOS spectra of individual QSOs reveal a strong and broad ~ 774 Å line in PG 1522+101 (also Cohen *et al.* 1994), and they support the prior claims of strong ~ 774 Å lines in PKS 0355–483 and Q 1435–015 (Hamann *et al.* 1995b). However, the new spectra contradict the report (based on old *IUE* data) that the ~ 774 Å line is strong in PG 1148+549 (Hamann *et al.* 1995a).

The centroids of the observed ~ 774 Å features support Ne VIII as the single most likely identification, but the velocity widths are significantly larger than O VI $\lambda 1034$ and all other BELs in two well-measured QSOs (PKS 0355–483 and PG 1522+101) and probably in the mean spectra. The ~ 774 Å line widths, ranging from FWHM $\approx 11,000$ to $15,000$ km s $^{-1}$, are ~ 2 to 5 times larger than the lower-ionization BELs. These ultra-broad profiles are consistent with significant contributions from N IV $\lambda 765$ and O IV $\lambda 789$ emission. However, photoionization calculations coupled with measurements of C IV $\lambda 1549$ constrain the N IV and O IV line strengths to be at least several times weaker than the average ~ 774 Å emission (§3.1.1). We conclude that exceptionally broad Ne VIII $\lambda 774$ dominates the average feature and is the only significant contributor when this line is strong compared to C IV $\lambda 1549$. The only way to avoid this conclusion is to invoke large line-of-sight velocity dispersions ($\gtrsim 1000$ km s $^{-1}$) in the BELR, so that the resonant absorption of continuum photons greatly enhances the N IV and O IV line strengths relative to both the continuum and C IV $\lambda 1549$ (§3.1.3). If Ne VIII dominates the ~ 774 Å emission, fits to the line profiles indicate that most of the flux comes from a distinct high-velocity region, with little or no contribution from the low-velocity gas responsible for C IV and the other lower-ionization lines (§3.2.1).

The photoionization calculations also indicate that the Ne VIII emitting regions have ionization param-

eters $5 \lesssim U \lesssim 30$, total column densities $10^{22} \lesssim N_H \lesssim 3 \times 10^{23}$ cm $^{-2}$, and covering factors $\gtrsim 30\%$ of 4π steradians (for solar abundances and a standard ionizing spectrum; §3.1.2). These results are uncertain by factors of a few because of the poorly known shape of the far-UV spectrum and the possible large contributions to the line fluxes from continuum pumping. Nonetheless, the Ne VIII component of the BELR must be considerably more ionized and probably more extensive than the regions producing lines like Ly α , Mg II $\lambda 2799$, and C IV $\lambda 1549$. The physical conditions in the Ne VIII emitting clouds are characteristic of the highly-ionized “warm” absorbers observed in soft X-rays, suggesting a close relationship between the BELR and the warm absorber gas. The Ne VIII emitting regions would themselves produce warm absorption (e.g. bound-free edges of O VII+O VIII at ~ 0.8 keV) if they lie along our line of sight to the X-ray continuum source.

We are grateful to G. J. Ferland for providing the CLOUDY software and R. Weymann for the reduced *HST* Key Project spectra. We also thank L. Zuo and D. Tytler for help with the Absnap data, G. J. Ferland, K. Korista and A. Laor for useful discussions, and R. Lyons for comments on this manuscript and help with the data processing. Finally, we thank an anonymous referee for helpful suggestions. This work was supported by NASA grants NAG 5-1630 and NAG 5-3234, and by the Space Telescope Science Institute through the archival grant AR-5292-93A and the Guest Observer grant GO-6103-94A.

TABLE 1
LOG OF OBSERVATIONS

Date	Tel.	Instr./Setup	λ_{obs}^a	R	Exp. ^a
PKS 0355–483 ($z_e = 1.005$)					
12 Feb. 1996	<i>HST</i>	FOS/BL–G160L	1140–2508	250	5440
12 Feb. 1996	<i>HST</i>	FOS/BL–G270H	2221–3301	1300	1090
PG 1148+549 ($z_e = 0.969$)					
15 Sep. 1995	<i>HST</i>	FOS/BL–G130H	1140–1606	1300	2860
15 Sep. 1995	<i>HST</i>	FOS/BL–G190H	1573–2330	1300	750
15 Sep. 1995	<i>HST</i>	FOS/BL–G270H	2221–3301	1300	350
Q 1435–015 ($z_e = 1.310$)					
21 Jan. 1996	<i>HST</i>	FOS/BL–G160L	1140–2508	250	2960
21 Jan. 1996	<i>HST</i>	FOS/BL–G270H	2221–3301	1300	720
30 Jul. 1995	Lick 3m	KAST–grismIII	3100–4415	1400	3000
PG 1522+101 ($z_e = 1.318$)					
14 Mar. 1992	<i>HST</i>	FOS/BL–G160L	1140–2508	250	5635
14 Mar. 1992	<i>HST</i>	FOS/RD–G190H	1573–2330	1300	9487
14 Mar. 1992	<i>HST</i>	FOS/RD–G270H	2221–3301	1300	2638
27 Mar. 1992	Lick 3m	KAST–grismIII	3250–4600	1400	3600
28 Mar. 1992	Lick 3m	KAST–grismIII	3150–4500	1400	3600

^a λ_{obs} is in Å and Exp. is in seconds.

TABLE 2
EMISSION LINE MEASUREMENTS^a

Line	λ_{rest} (Å)	REW (Å)	Flux ^b	$\Delta\lambda$ (Å)	FWHM (km s ⁻¹)
Total Mean (16 spectra)					
Ne VIII λ 774	776.3	7.5	0.51	745–804	15,300
N III + C III	982.0	5.0	0.31	963–997	...
O VI λ 1034	1032.0	16.0	1.00	997–1057	6200
???	1070.9	3.5	0.22	1057–1090	...
Ly α + N V + Si II	1221.3	87.0	5.2	1160–1290	...
KP-full Mean (11 spectra)					
Ne VIII λ 774	776.3	5.9	0.42	745–804	14,800
N III + C III	982.0	4.6	0.30	963–997	...
O VI λ 1034	1030.8	15.3	1.00	997–1057	6500
???	1070.5	2.8	0.18	1057–1090	...
Ly α + N V + Si II	1220.8	85.9	5.3	1160–1290	...
Absnap Mean (5 spectra)					
Ne VIII λ 774	776.5	10.5	0.85	748–803	11,200
N III + C III	982.8	6.0	0.44	961–1001	...
O VI λ 1034	1033.9	13.5	1.00	1001–1057	5700
???	1073.2	4.3	0.32	1057–1095	...
Ly α + N V + Si II	1221.0	84.2	5.9	1160–1290	...
PKS 0355–483 ($z_e = 1.005$)					
Ne VIII λ 774	773.9	13.8	9.3	748–800	14,100
N III + C III	987.9	6.5	4.0	967–1004	...
O VI λ 1034	1034.7	10.6	6.4	1017–1049	3750
Ly α + N V + Si II	1225.9	67.5	36.5	1193–1283	...
Si IV + O IV]	1402.8	4.1	1.9	1377–1429	...
C IV λ 1549	1551.6	8.3	3.4	1536–1575	2500
PG 1148+549 ($z_e = 0.969$)					
Ne VIII λ 774	772.4	4.0:	3.4:	743–801	...
N III + C III	983.1	4.9:	3.5:	962–1000	...
O VI λ 1034	1025.5	14.2	9.9	1000–1047	8500
Ly α + N V + Si II	1219.7	89.5	53.2	1155–1275	...
Si IV + O IV]	1398.7	10.0	4.7	1373–1418	...
C IV λ 1549	1540.8	35.1	17.8	1488–1586	7400

TABLE 2—*Continued*

Line	λ_{rest} (Å)	REW (Å)	Flux ^b	$\Delta\lambda$ (Å)	FWHM (km s ⁻¹)
Q 1435–015 ($z_e = 1.310$)					
Ne VIII $\lambda 774$	775.6	5.4	4.1	746–805	11,000:
N III + C III	977.6	6.6	4.6	951–998	...
O VI $\lambda 1034$	1031.1	11.2	7.7	1003–1059	6800:
Ly α + N V + Si II	1219.3	62.7	41.1	1165–1283	...
Si IV + O IV]	1397.3	4.2	2.3	1370–1425	...
C IV $\lambda 1549$	1546.5	26.0	13.7	1476–1597	4200
PG 1522+101 ($z_e = 1.318$)					
Ne VIII $\lambda 774$	776.1	13.5	12.1	739–808	15,000
O VI $\lambda 1034$	1032.2	17.0	16.9	998–1063	7200
Ly α + N V + Si II	1224.2	63.1	58.5	1166–1287	...
Si IV + O IV]	1406.6	10.1	8.3	1368–1439	...
C IV $\lambda 1549$	1544.8	27.1	20.8	1489–1592	6500

^aWavelengths and REWs are relative to the redshifts listed.

^bFluxes are relative to O VI $\lambda 1034$ for the mean spectra and as observed with units 10^{-14} ergs s⁻¹ cm⁻² for the individual QSOs.

REFERENCES

- Bahcall, J. N., *et al.* 1993, ApJS, 87, 1
- Baldwin, J. 1977, ApJ, 214, 679
- Baldwin, J. A., Ferland, G. J., Hamann, F., Carswell, R., Phillips, M., Wilkes, B., & Williams, R. E. 1996, ApJ, 461, 664
- Cardelli, J. A., Clayton, G. C., & Mathis, J. S. 1989, ApJ, 345, 245
- Cohen, R., Beaver, E. A., Burbidge, E. M., Hamann, F., Junkkarinen, V. T., & Lyons, R. W. 1994, in Poster Papers accompanying *The Analysis of Emission Lines*, ed. M. Livio, STScI Symposium, (Cambridge:New York) 10
- Crenshaw, D. M., Bruegman, O. W., & Norman, D. J. 1990, PASP, 102, 463
- Davidson, K., & Netzer, H. 1979, Rev. Mod. Phys., 51, 715
- Diplas, A., & Savage, B. D. 1994, ApJ, 427, 274
- Espey, B. R., Carswell, R. F., Bailey, J. A., Smith, M. G., & Ward, M. J. 1989, ApJ, 342, 666
- Fabian, A. C. *et al.* 1994, PASJ, 46, L59
- Ferguson, J. W., Ferland, G. J., & Pradhan, A. K. 1995, ApJ, 438, L55
- Ferland, G. J. 1996 *HAZY, a Brief Introduction to Cloudy*, University of Kentucky, Department of Physics and Astronomy, Internal Report
- Ferland, G. J., Korista, K. T., & Peterson, B. M. 1990, ApJ, L21
- Ferland, G. J., Peterson, B. M., Horne, K., Welsch, W. F., & Nahar, S. N. 1992, ApJ, 387, 95
- Fiore, F., Elvis, M., Mathur, S., Wilkes, B. J., & McDowell, J. 1993, ApJ, 415, 129
- Foltz, C. B., Chaffee Jr., Weymann, R. J., & Anderson, S. F. 1988, in *QSO Absorption Lines: Probing the Universe*, eds. J. C. Blades, D. A. Turnshek, & C. A. Norman (Cambridge: Cambridge Univ. Press), p. 53
- George, I. M., Turner, T. J., Netzer, H., Nandra, K., Mushotzky, R. F., & Yaqoob, T. 1997, ApJS, in press
- George, I. M., Turner, T. J., & Netzer, H. 1995, ApJ, 438, L67
- Halpern, J. P. 1984, ApJ, 281, 90
- Hamann, F., Barlow, T. A., Beaver, E. A., Burbidge, E. M., Cohen, R. D., Junkkarinen, V., & Lyons, R. 1995c, ApJ, 443, 606
- Hamann, F., & Ferland, G. J. 1992, ApJ, 391, L53
- Hamann, F., & Ferland, G. J. 1993, ApJ, 418, 11
- Hamann, F., & Korista, K. T. 1996, ApJ, 464, 158
- Hamann, F., Shields, J. C., Cohen, R. D., Junkkarinen, V. T., & Burbidge, E. M. 1996, in "Emission Lines in Active Galaxies," (I.A.U Colloquium 159, Shanghai, China), eds. B. Peterson, F.-Z. Cheng, and A. S. Wilson, (ASP Conf. Series), 96
- Hamann, F., Shields, J. C., Ferland, G. J., & Korista, K. 1995a, ApJ, 454, 688
- Hamann, F., Zuo, L., & Tytler, D. 1995b, ApJ, 444, L69
- Hewitt, D. & Burbidge, G. 1993, ApJS, 87, 451
- Kinney, A. L., Rivolo, A. R., & Koratkar, A. R. 1990, ApJS, 75, 645
- Kinney, A. L., Bohlin, R. C., Blades, J. C., & York, D. G. 1991, ApJS, 75, 645
- Korista, K., Baldwin, J., Ferland, G., & Verner, D. 1997, ApJS, 108, 401
- Kwan, J., & Krolik, J. 1981, ApJ, 250, 478
- Lanzetta, K. M., Turnshek, D. A., & Sandoval J. 1993, ApJS, 84, 109
- Laor, A., Jannuzi, B. T., Green, R. F., & Boroson, T. A. 1997a, ApJ, in press
- Laor, A., Bahcall, J. N., Jannuzi, B. T., Schneider, D. P., Green, R. F., & Hartig, G. F. 1994, ApJ, 420, 110
- Laor, A., Bahcall, J. N., Jannuzi, B. T., Schneider, D. P., Green, R. F., & Hartig, G. F. 1995, ApJS, 99, 1
- Laor, A., Fiore, F., Elvis, M., Wilkes, B. J., & McDowell, J. C. 1997b, ApJ, 477, 93

- Marziani, P., & Sulentic, J. W. 1993, ApJ, 409, 612
- Mathews, W. G., & Ferland, G. J. 1987, ApJ, 323,456
- Mathur, S. 1994, ApJ, 431, L75
- Mathur, S., Elvis, M., & Singh, K. P. 1995, ApJ, 455, L9
- Mathur, S., Wilkes, B., Aldcroft, T. 1997, ApJ, in press
- Mathur, S., Wilkes, B., Elvis, M., & Fiore, F. 1994, ApJ, 434, 493
- McDowell, J. C., Canizares, C., Elvis, M., Lawrence, A., Markoff, S., Mathir, S., & Wilkes, B. J. 1995, ApJ, 450, 585
- Mihara, T., Matsuoka, M., Mushotzky, R. F., Kunieda, H., Otani, C., Miyamoto, S., & Yamauchi, M. 1994, PASJ, 46, L59
- Murphy, E. M., Lockman, F. J., Laor, A., & Elvis, M. 1996, ApJS, 105, 369
- Murray, N. 1996, private comm.
- Murray, N., & Chiang, J. 1995, ApJ, 454, L105
- Murray, N., Chiang, J., Grossman, S. A., & Voit, G. M. 1995, 451, 498
- Nandra, K., & Pounds, K. A. 1994, MNRAS, 268, 405
- Netzer, H. 1993, ApJ, 411, 594
- Netzer, H. 1996, ApJS, 473, 781
- Nichols, J. S., & Linsky, J. L. 1996, AJ, 111, 517
- Osterbrock, D. E. 1986, ARA&A, 24, 171
- Osterbrock, D. E. 1989, *Astrophysics of Gaseous Nebulae and Active Galactic Nuclei*, (Mill Valley:University Science Books)
- Otani, C., *et al.* 1996, PASJ, 48, 211
- Reynolds, C. S. 1997, MNRAS, 286, 513
- Reynolds, C. S., & Fabian, A. C. 1995, MNRAS, 273, 1167
- Schmidt, M., & Green, R. F. 1983, ApJ, 269, 352
- Schneider, D. P., *et al.* 1993, ApJS, 87, 45
- Shields, J. C., & Ferland, G. J. 1993, ApJ, 402, 425
- Shields, J. C., Ferland, G. J., & Peterson, B. M. 1995, ApJ, 441, 507
- Shields, J. C., & Hamann, F. 1997, ApJ, 481, 752
- Turner, T. J., & Pounds, K. A. 1989, MNRAS, 240, 833
- Turner, T. J., George, I. M., & Mushotzky, R. F. 1993b, ApJ, 412, 72
- Turner, T. J., Nandra, K., George, I. M., Fabian, A. C., & Pounds, K. A. 1993a, ApJ, 419, 127
- Tytler, D., & Fan, X.-M. 1992, ApJS, 79, 1
- Tytler, D., & Zuo, L. 1994, private comm.
- Ulrich, M. H. 1988, MNRAS, 230, 121
- Verner, D., Verner, E. M., & Ferland, G. J. 1996, Atomic Data and Nuclear Data Tables, 64, 1
- Weymann, R. J., Morris, S. L., Foltz, C. B., & Hewett, P. C. 1991, ApJ, 373, 23
- Wiese, W. L., Smith, M. W., & Glennon, B. M. 1966, Atomic Transition Probabilities (NBS-NSRDS 4, vol. 1) (Washington: GPO)
- Wills, B. J., *et al.* 1995, ApJ, 447, 139
- Zheng, W., Kriss, G. A., Telfer, R.C., Grimes, J. P., & Davidson, A. F. 1997, ApJ, 475, 469

Figure Captions

Fig. 1.— *HST*-FOS spectra of PKS 0355–483. The “Absnap” spectrum is from Hamann *et al.* (1995b). The “new *HST*” spectrum (this paper) is shifted vertically by adding 3.5 in these F_λ flux units, 10^{-15} ergs $\text{s}^{-1} \text{cm}^{-2} \text{\AA}^{-1}$. The narrow peak in Ly α is due at least partly to geocoronal Ly α emission in second order at $\sim 2435 \text{\AA}$. Both spectra are smoothed twice with a 3-pixel-wide boxcar function. The dotted curve is a fit to the continuum. Various possible emission lines are labeled at the redshift given in the tables; not all of these lines are present. See §2.1.

Fig. 2.— *HST*-FOS and *IUE* spectra of PG 1148+549. The “*HST*” and “new *IUE*” spectra are shifted up by adding 22.0 and 11.0, respectively. The *IUE* spectra are smoothed twice and the *HST* spectrum 4 times with a 3-pixel-wide boxcar function. The spike at 1663\AA in the new *IUE* spectrum is a camera artifact. The old and new *IUE* spectra are different reductions of the same data. See Figure 1 and §2.1.

Fig. 3.— *HST*-FOS spectra of Q 1435–015. The “new *HST* + Lick” spectrum is shifted up by adding 2.5, and both *HST* spectra are smoothed twice with a 3-pixel-wide boxcar function. See Figure 1 and §2.1.

Fig. 4.— *HST*-FOS and Lick Observatory spectra of PG 1522+101. The G160L spectrum is shifted up by adding 3.3. The high-resolution spectrum is smoothed by 3 applications of a 3-pixel-wide boxcar function. Weak Lyman limit absorption at $\sim 1980 \text{\AA}$ affects the continuum shape. See Figure 1 and §2.1.

Fig. 5.— Mean *HST*-FOS spectra of QSOs in the Absnap, KP-sub, KP-full and Total samples (see §2.2). The lines are labeled at their rest wavelengths. The continua are normalized to unity but shifted vertically by adding 1.0 to the KP-sub mean, 2.0 to KP-full and 3.0 to the Total. The dotted curves show the estimated continuum levels. The histogram at the bottom shows the number of spectra contributing to the Total mean at each wavelength.

Fig. 6.— Predicted line equivalent widths (W_λ in \AA) for photoionized emitting regions that completely cover the central continuum source (over 4π steradians). Each value of the ionization parameter represents a different region/calculation. The equivalent

widths can be converted to relative fluxes by scaling by the continuum slope across these wavelengths, $F_\lambda \propto \lambda^{-1.5}$. See §3.1.

Fig. 7.— Line profiles in PKS 0355–483 (solid curves, as labeled) are compared to C IV $\lambda 1549$ (dotted curve in all panels). Zero velocity is defined by the emission redshift given in Table 1, assuming rest wavelengths weighted 2:1 for the doublets C IV $\lambda\lambda 1548, 1551$, N V $\lambda\lambda 1239, 1243$ and O VI $\lambda\lambda 1032, 1038$. Open brackets mark the positions of the individual doublet members. The C IV doublet separation (not shown) is 500 km s^{-1} . The velocity scale in the bottom panel applies to Ly α 1215.67\AA . The spectra are normalized to unity in the continuum and smoothed by 1 application of a 3-pixel-wide boxcar function. See §3.2.1.

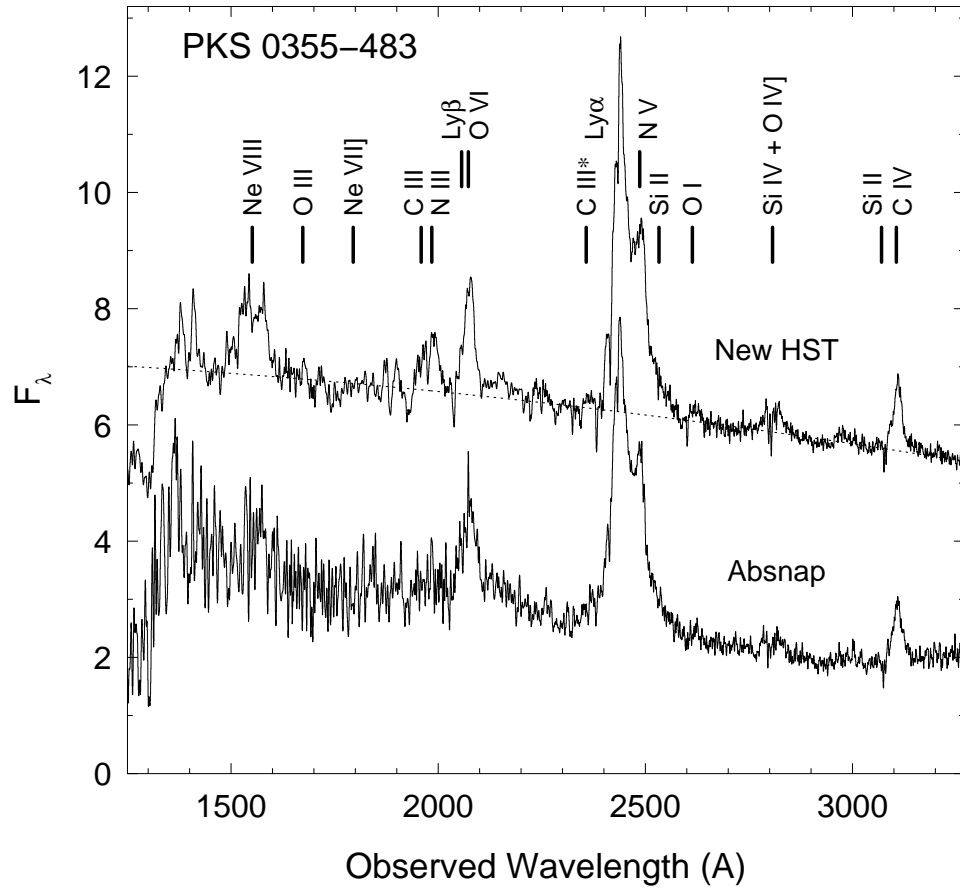
Fig. 8.— Same as Figure 7 but for PG 1522+101.

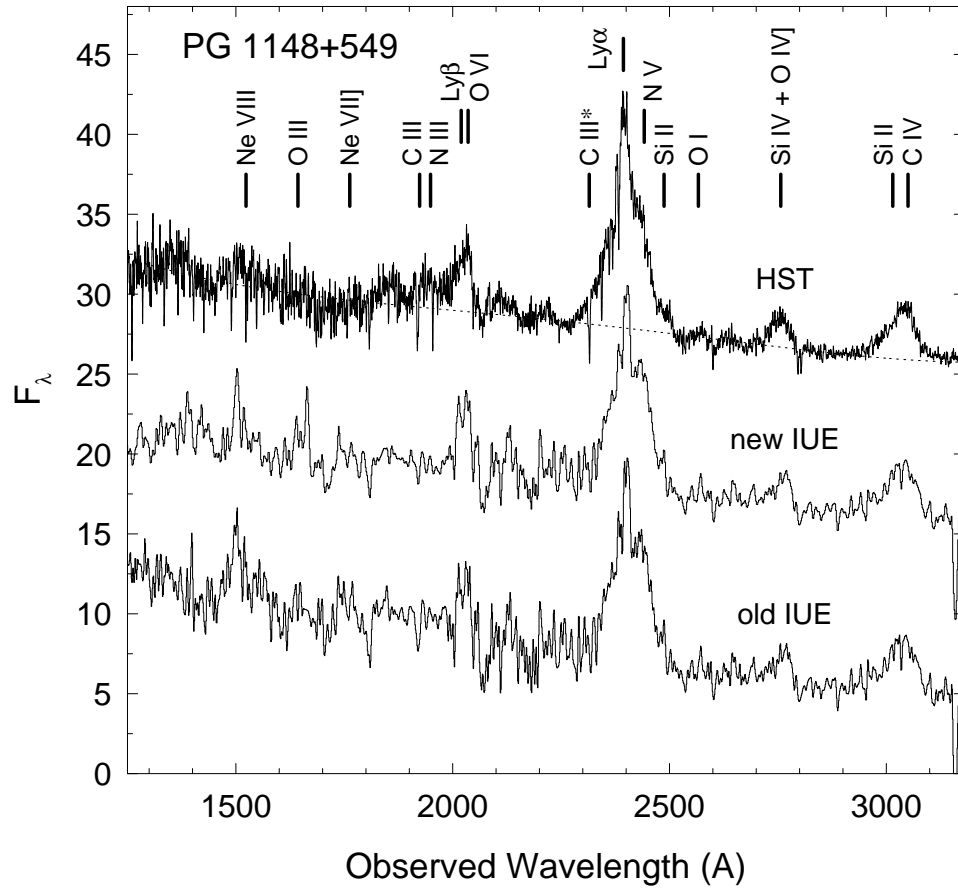
Fig. 9.— Same as Figure 7 but for Q 1435–015.

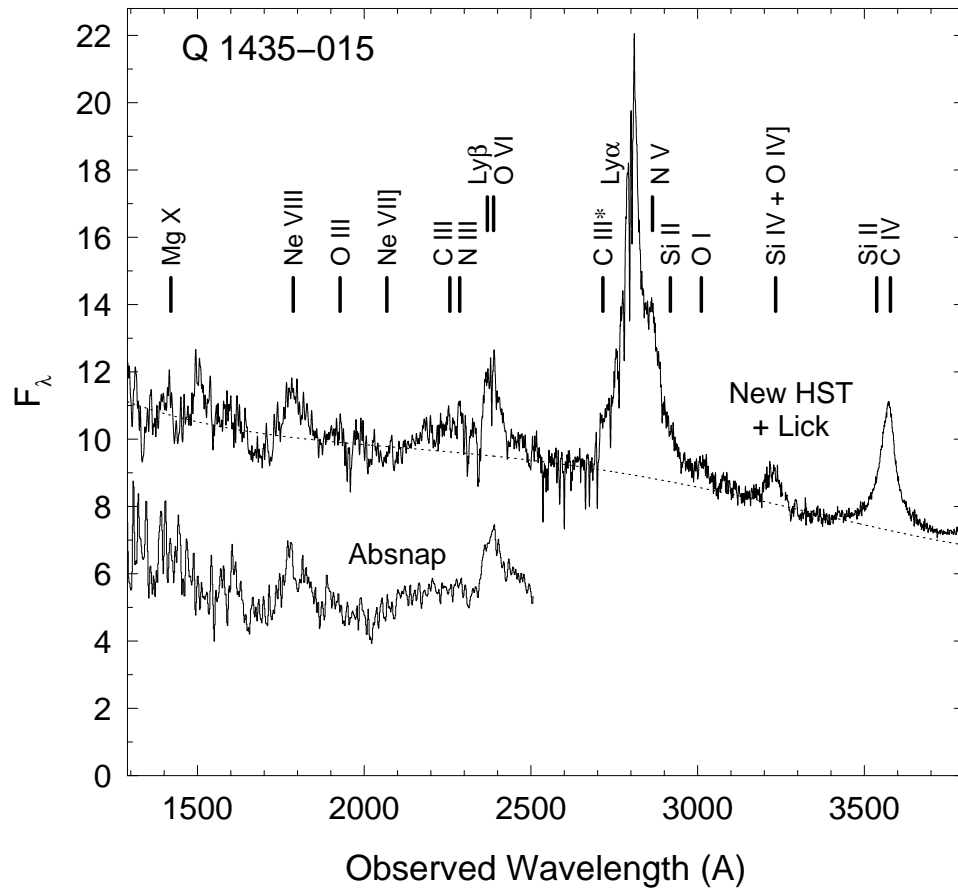
Fig. 10.— Ne VIII $\lambda 774$ line profile (bold curve in all panels) measured in PKS 0355–483 is compared to various fits (thin curves) that use the C IV $\lambda 1549$ profile as a template. The lines contributing to the fits are indicated in each panel, with tic marks across the bottom showing their centroid positions. See Figure 7 and §3.2.1.

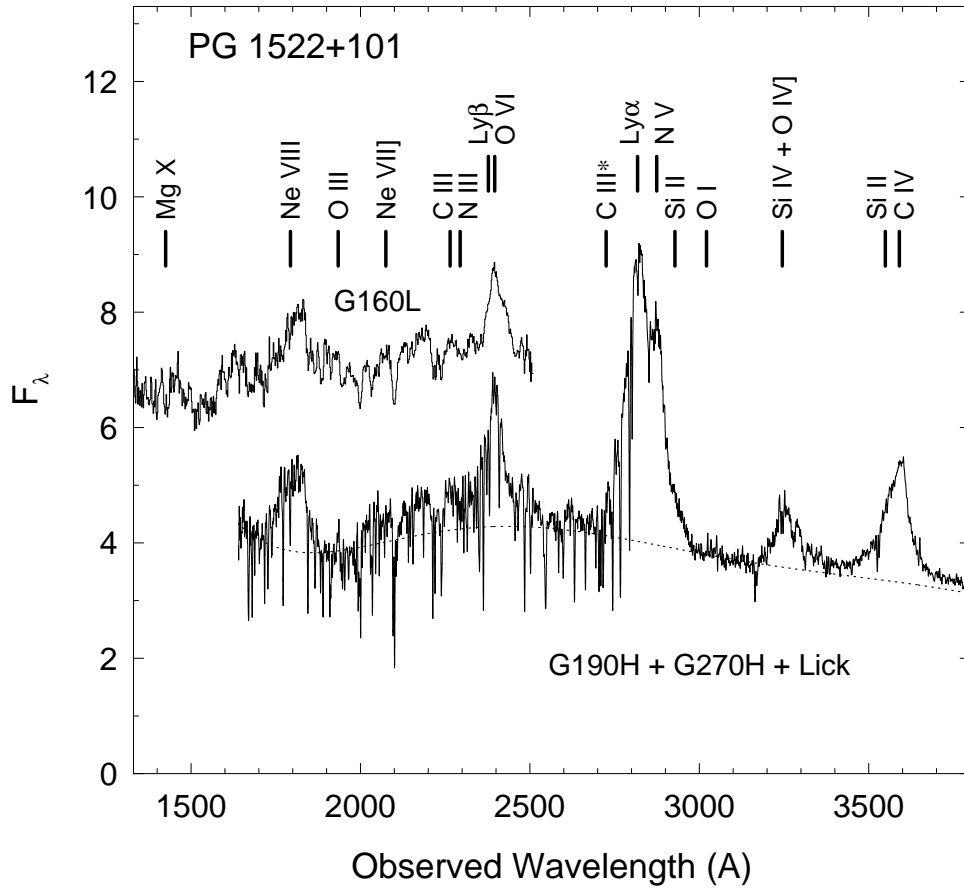
Fig. 11.— Same as Figure 9 but for PG 1522+101.

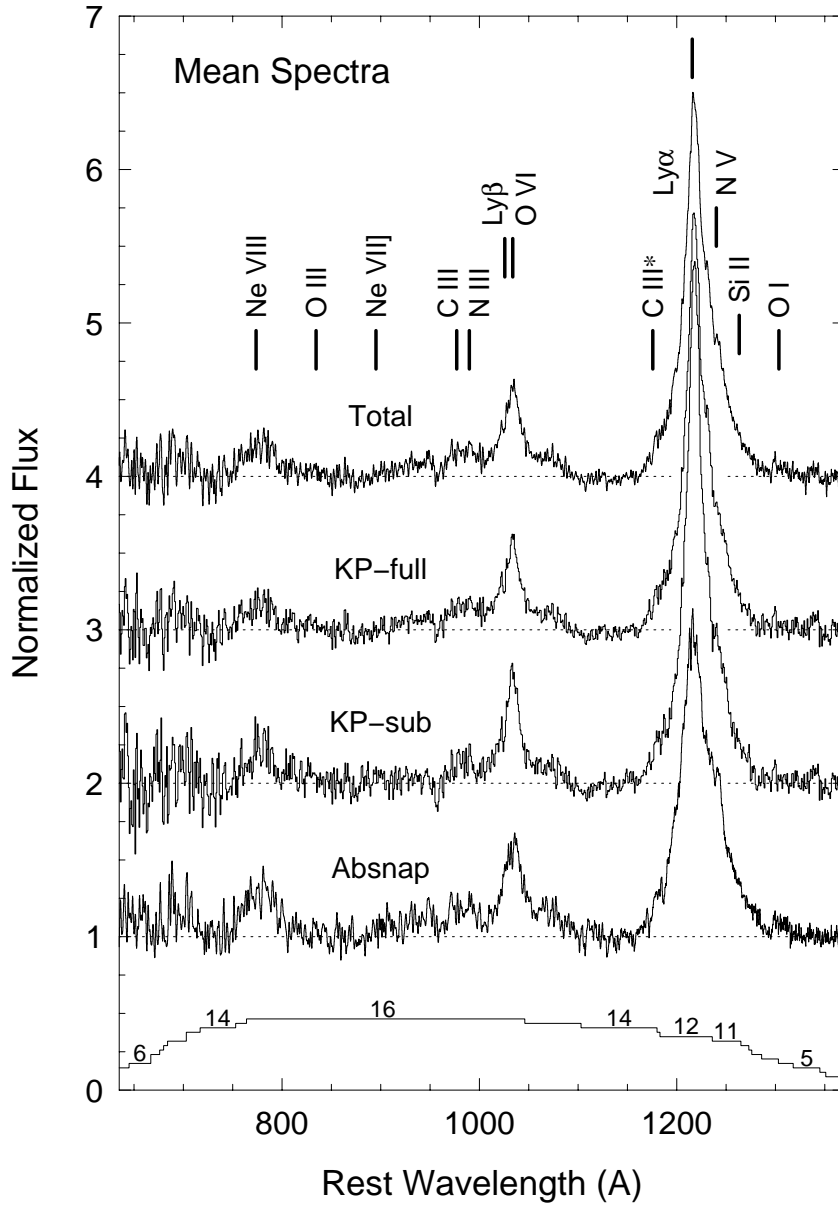
Fig. 12.— Measured Ne VIII $\lambda 774$ line profiles (bold curves) in PKS 0355–483 and PG 1522+101 are compared to gaussian fits (one gaussian per doublet component). The thin solid line shows the overall fit, while the dotted lines show the individual components. The component centroids are shown by tic marks at the bottom of each plot. See §3.2.1.

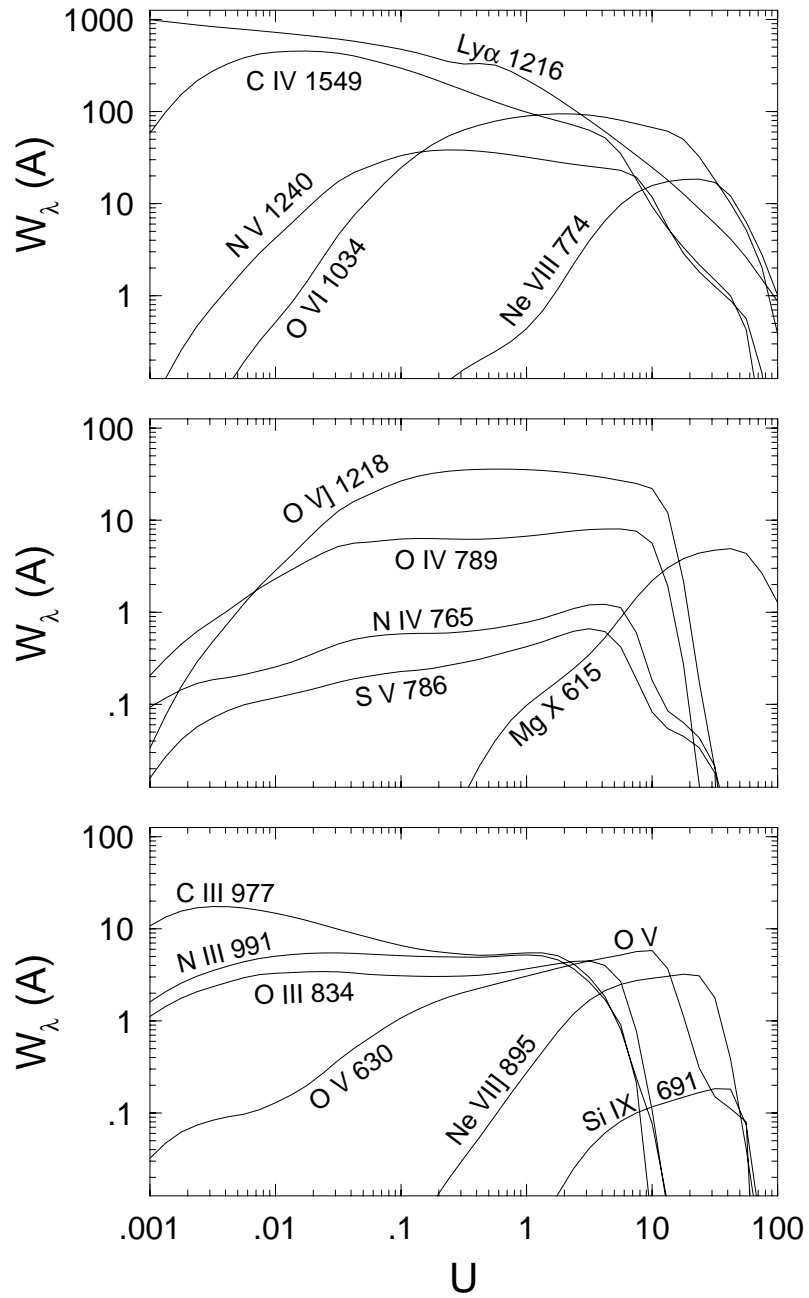




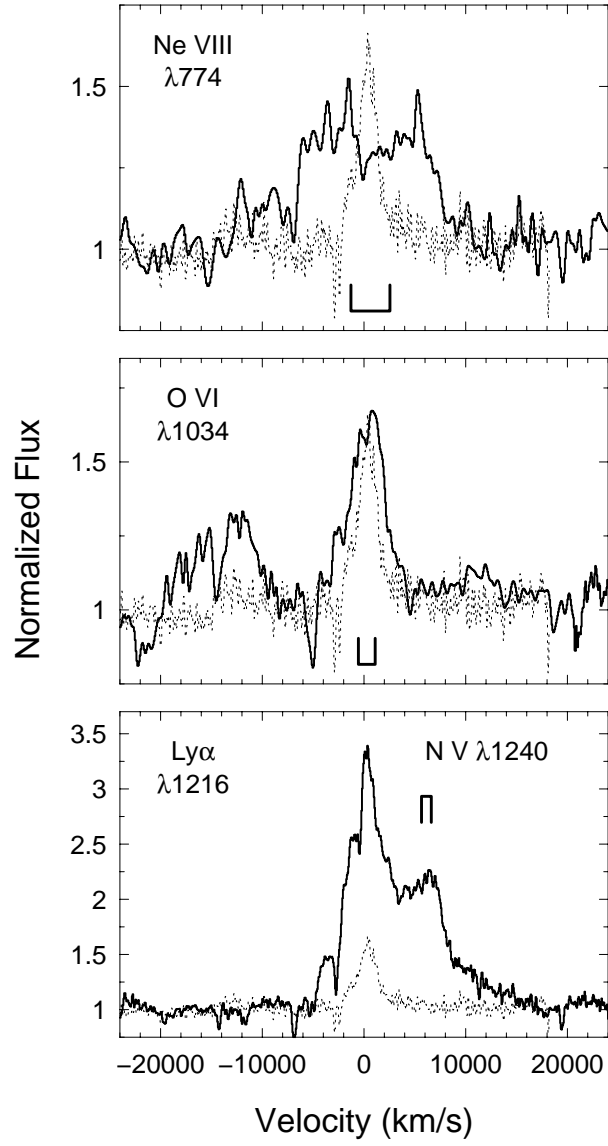




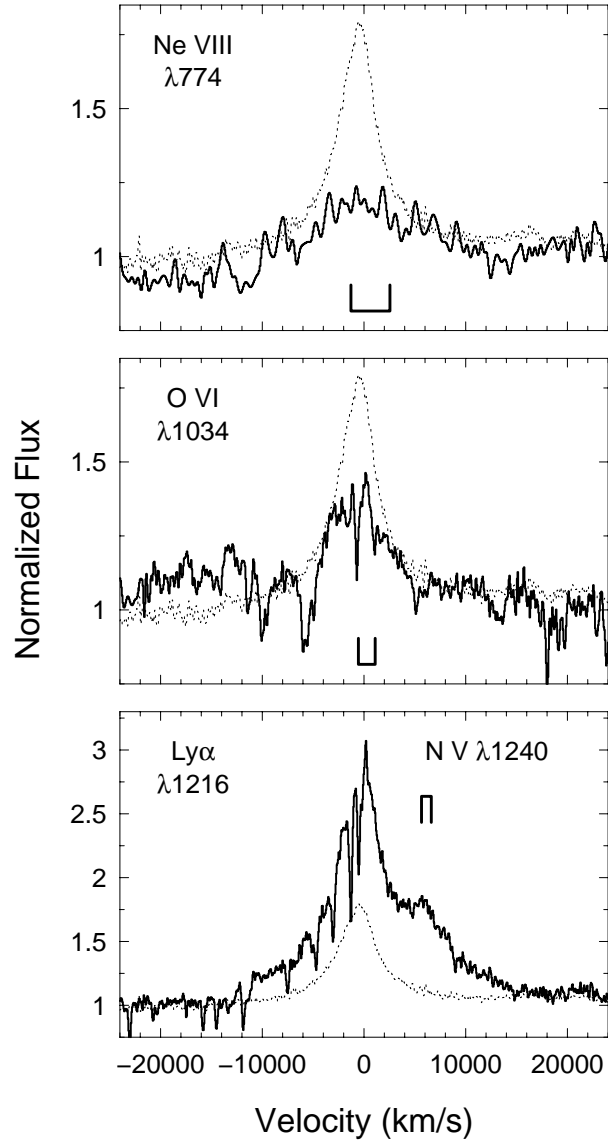




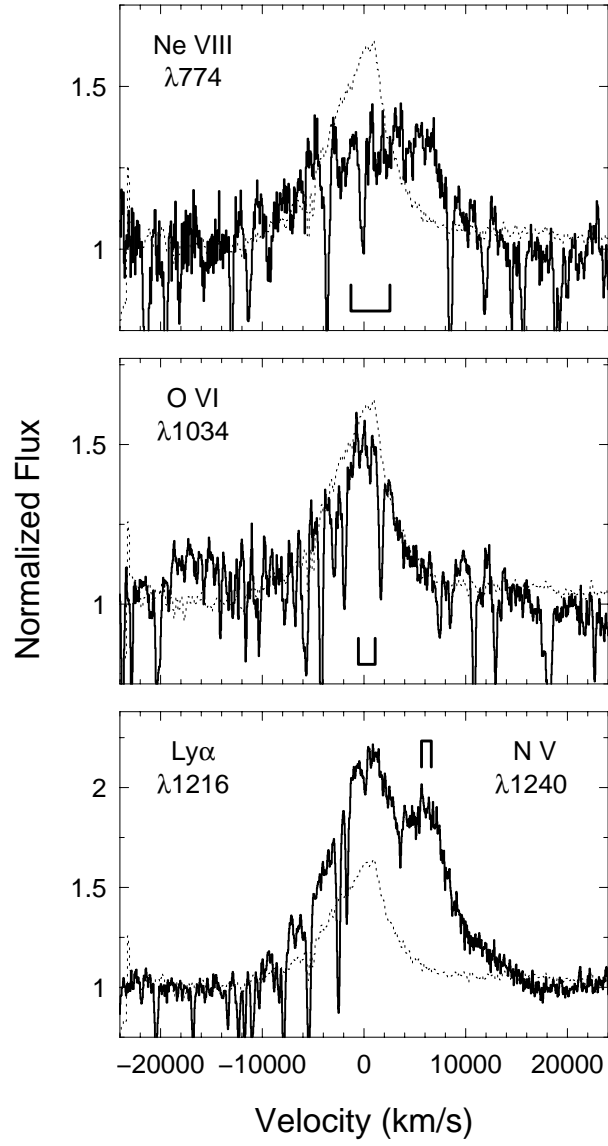
PKS 0355-483



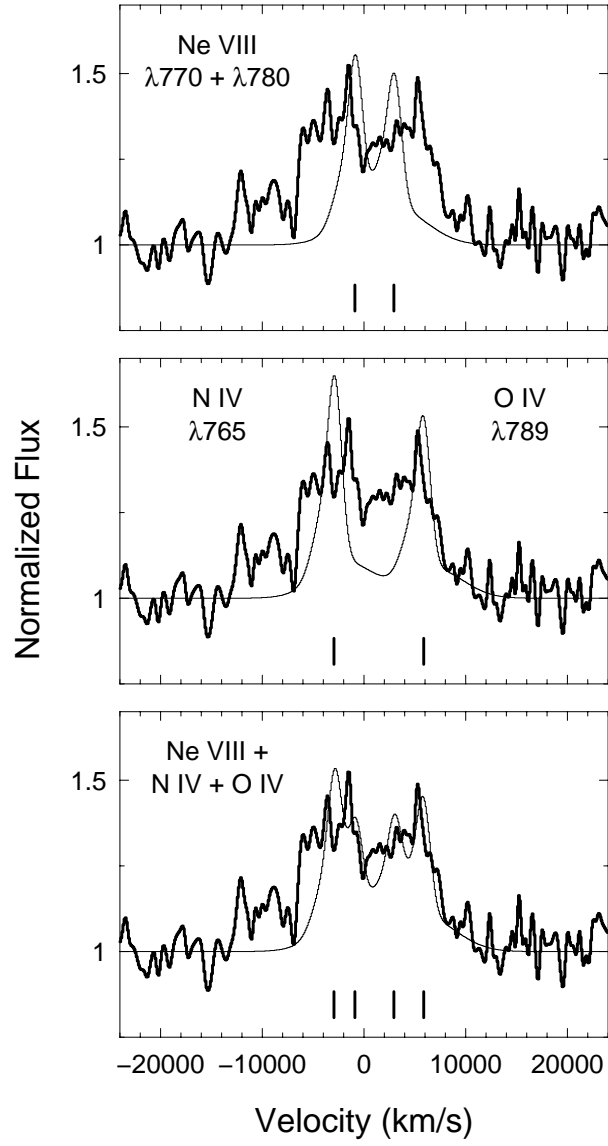
Q 1435-015



PG 1522+101



PKS 0355-483



PG 1522+101

